Optimization of flux-surface density variation in stellarator plasmas with respect to the transport of collisional impurities

(article starts on next page)

Optimization of flux-surface density variation in stellarator plasmas with respect to the transport of collisional impurities

S. Buller,[1, a)] H.M. Smith,[2] A. Mollén,[2] S.L. Newton,[3, 1] and I. Pusztai[1]

[1)] *Department of Physics, Chalmers University of Technology, SE-41296 Göteborg,*
Sweden
[2)] *Max-Planck-Institut für Plasmaphysik, 17491 Greifswald,*
Germany
[3)] *CCFE, Culham Centre for Fusion Energy, Abingdon, Oxon OX14 3DB,*
UK

Avoiding impurity accumulation is a requirement for steady-state stellarator oper-ation. The accumulation of impurities can be heavily affected by variations in their density on the flux-surface. Using recently derived semi-analytic expressions for the transport of a collisional impurity species with high-Z and flux-surface density-variation in the presence of a low-collisionality bulk ion species, we numerically optimize the impurity density-variation on the flux-surface to minimize the radial peaking factor of the impurities. These optimized density-variations can reduce the core impurity density by 0.75^Z (with Z the impurity charge number) in the Large Helical Device case considered here, and by 0.89^Z in a Wendelstein 7-X stan-dard configuration case. On the other hand, when the same procedure is used to find density-variations that maximize the peaking factor, it is notably increased compared to the case with no density-variation. This highlights the potential im-portance of measuring and controlling these variations in experiments.

Keywords: fusion plasmas, collisional transport, stellarators, impurity transport

I. INTRODUCTION

Highly-charged impurities can enter fusion plasmas from the walls of the vessel. In any magnetic-confinement fusion-reactor, these impurities must be prevented from accumulating in the core of the plasma, where they radiate strongly and lead to unsustainable energy losses.

Impurity accumulation is one of the major challenges in stellarators[1], where it is often observed when the radial electric field points inwards[1–4], which occurs when the electron and ion temperatures are comparable[5], and is a preferred regime for future reactors[6].

Such accumulation is also predicted theoretically, based on collisional transport calcula-tions with simplified pitch-angle scattering collision operators. However, such simplified op-erators are not appropriate for treating highly-charged impurities with high collisionality[7]. When an appropriate collision operator is used, the radial transport of the heavy impurities becomes insensitive to the radial electric field[7–9]. Additionally, if the bulk ions are in a low-collisionality regime, impurity accumulation can be avoided by having large temperature gradients[7,9] – an effect known as *temperature screening*.

However, these results do not account for the tendency of highly-charged impurities to develop density-variations on the flux-surface[10–12]. Such variations occur when any plasma-species deviates from a flux-surface Maxwell-Boltzmann distribution, and are strongest for highly-charged species. When these variations are accounted for, the radial electric field again affects the transport of heavy-impurities[13,14]. In most scenarios, this leads to an

a)Electronic mail: bstefan@chalmers.se

accumulation of impurities[13,14], but there exist cases where the radial electric field is mildly beneficial: In Ref. 13, where the density variation is due to electrostatic potential-variation from trapped-particles[15] – calculated with the EUTERPE code – there exists a narrow range of inward radial-electric fields that lead to an outward impurity flux for one of the charge states ($Z = 24$, the lowest charge state investigated). In Ref. 14, where a model of a localized flux-surface variation of impurities was considered, it was found that an inward radial-electric field can lead to weak outward transport if the amplitude of the localized variation is small. Furthermore, the outward transport of carbon impurities can be enhanced by electrostatic potential-variations caused by fast, perpendicularly injected, neutral-beam particles[16].

Thus, it is in some cases possible for flux-surface density variations to reduce or prevent impurity accumulation. The aim of the present work is to theoretically explore what beneficial impurity density variations look like, and by how much they can reduce impurity accumulation. We do this by optimizing the radial transport of impurities with respect to the impurity density variation, based on semi-analytical expressions for the impurity transport coefficients from Ref. 14. In particular, we look at variations that lead to the least (or most) impurity accumulation. These expressions account for the classical and neoclassical transport; recent studies indicate that turbulent transport may be significant for the impurities[17]. However, for highly charged impurities, even if the diffusive part of the transport is dominated by turbulence (as found in Ref. 17), the convective part of the transport (i.e. the one independent of the impurity density gradient) – that determines the sign of the peaking factor – can still be dominated by collisional transport, as it increases with Z. We do not include turbulent transport in this work, but note that it is also affected by flux surface variations[18,19].

The remainder of this paper is organized as follows: in the next section, we present the mathematical formulation of the problem and analytic expressions for the impurity transport coefficients, radial flux and peaking factor. In Sec. II A, we explain how the impurity density variation is represented and optimized. In Sec. III, we present the results of such optimization applied to model cases based on Wendelstein 7-X (W7-X) and Large Helical Device (LHD) profiles and magnetic geometries. These initial explorations indicate that tuning the impurity density variations could be useful in reducing core impurity accumulation. Further work is however needed to assess how the presence of turbulence would affect the results.

II. MATHEMATICAL FORMULATION

In this section, we describe the radial transport of a highly-charged collisional impurity species (labeled "z") due to collisions with a bulk-ion species (labeled "i"). Specifically, we consider a *mixed-collisionality* regime[7] where the impurities are collisional and the bulk ions are in the $1/\nu$ regime. The impurities are not restricted to the trace limit, but are assumed to be highly charged, with charge Ze, where $Z \gg 1$ and e is the proton charge. We here summarize results from Ref. 14, which is a generalization of Refs. 10–12 from tokamaks to stellarators, and a generalization of Refs. 7,9 for impurities varying on the flux surface.

The parallel momentum equation of a collisional impurity species is

$$T\nabla_\| n_z = -Zen_z\nabla_\|\Phi + R_{z\|},\tag{1}$$

where T is the impurity temperature, which is equilibrated with the main ion temperature $T_i = T$; $\nabla_\|$ denotes the gradient projected onto the magnetic field direction; n_z is the impurity density, which varies along the flux-surface; Φ the electrostatic potential; and $R_{z\|}$ the parallel friction force. In the mixed-collisionality regime, the friction force is smaller than the other terms in this equation, which results in

$$n_z = N_z(r_N)\exp\left(-\frac{Ze\tilde{\Phi}}{T}\right),\tag{2}$$

where r_N is a flux-surface label (in this paper, $r_N = \sqrt{\psi_t/\psi_{t,\mathrm{LCFS}}}$, where ψ_t is the toroidal flux and $\psi_{t,\mathrm{LCFS}}$ the toroidal flux at the last-closed flux-surface); N_z is a flux-function known as the *pseudo-density*; and $\tilde{\Phi}$ is the deviation of Φ from its flux-surface average. The form of the density in (2) is known as the *Boltzmann-response* to the electrostatic potential, and is the equilibrium density in confined plasmas. If all species in the plasma obeyed (2), quasi-neutrality would force Φ to be a flux-function, and all densities would be constant along the flux-surface. However, if any species deviate from (2), Φ will vary on the flux-surface, which can cause species with high Z to develop significant density-variations on the flux-surface.

Assuming that (2) holds for the impurities – regardless of the mechanism that causes the Φ variation – the collisional radial transport of the impurities in the mixed-collisionality regime can be written as

$$
\begin{aligned}
\frac{\langle \mathbf{\Gamma}_z \cdot \nabla r_{\mathrm N} \rangle}{\langle n_z \rangle} = & - D_{N_z}[n_z]\frac{1}{Z}\frac{\mathrm d \ln N_z}{\mathrm d r_{\mathrm N}} + D_\Phi[n_z]\frac{e}{T}\frac{\mathrm d \langle \Phi \rangle}{\mathrm d r_{\mathrm N}} \\
& - D_{n_i}[n_z]\frac{\mathrm d \ln n_i}{\mathrm d r_{\mathrm N}} - D_{T_i}[n_z]\frac{\mathrm d \ln T}{\mathrm d r_{\mathrm N}},
\end{aligned}
\tag{3}
$$

where $\langle \cdot \rangle$ denotes the flux-surface average. In (3) the transport coefficients $D_X[n_z]$ depend on the impurity-variation on the flux-surface, as indicated by the square-brackets. Specifically,

$$
\frac{D_{N_z}}{D} = \langle n_z w^2 B^2 \rangle - \langle n_z w B^2 \rangle \frac{\langle w B^2 \rangle}{\langle B^2 \rangle} + \frac{\frac{\langle n_z w B^2 \rangle}{\langle B^2 \rangle}\left\langle \frac{B^2}{n_z} \right\rangle - \langle w B^2 \rangle}{\left\langle \frac{B^2}{n_z}(1 - c_4 \alpha) \right\rangle} \langle (1 - c_4 \alpha) w B^2 \rangle + \left\langle \frac{n_z |\nabla r_N|^2}{B^2} \right\rangle,
\tag{4}
$$

$$
\frac{D_{n_i}}{D} = - \langle n_z w u B^2 \rangle + \langle n_z w B^2 \rangle \frac{\langle u B^2 \rangle}{\langle B^2 \rangle} - \frac{\frac{\langle n_z w B^2 \rangle}{\langle B^2 \rangle}\left\langle \frac{B^2}{n_z} \right\rangle - \langle w B^2 \rangle}{\left\langle \frac{B^2}{n_z}(1 - c_4 \alpha) \right\rangle} \left(c_2 + \langle u B^2 \rangle [c_1 + 1] \right) - \left\langle \frac{n_z |\nabla r_N|^2}{B^2} \right\rangle,
\tag{5}
$$

$$
\frac{D_{T_i}}{D} = \frac{1}{2} \langle n_z w u B^2 \rangle - \frac{1}{2} \langle n_z w B^2 \rangle \frac{\langle u B^2 \rangle}{\langle B^2 \rangle} - \frac{\frac{\langle n_z w B^2 \rangle}{\langle B^2 \rangle}\left\langle \frac{B^2}{n_z} \right\rangle - \langle w B^2 \rangle}{\left\langle \frac{B^2}{n_z}(1 - c_4 \alpha) \right\rangle} \left(c_3 - \frac{3}{2} c_2 - \langle u B^2 \rangle \left[c_1(\eta - 1) + \frac{1}{2} \right] \right)
\tag{6}
$$

$$
+ \frac{1}{2} \left\langle \frac{n_z |\nabla r_N|^2}{B^2} \right\rangle,
$$

$$
D_\Phi = - D_{n_i} - D_{N_z},
\tag{7}
$$

where $D = \frac{m_i n_i T_i}{Z e^2 \langle n_z \rangle n_z \tau_{iz}}$; $\alpha = Z^2 n_z / n_i$; $\eta \approx 1.17$; c_1 to c_4 are flux-surface constants that depend on the magnetic geometry and n_z, defined in the Appendices A–D of Ref. 14; and

$$
\mathbf{B} \cdot \nabla u = - \mathbf{B} \times \nabla \psi \cdot \nabla(B^{-2}),
\tag{8}
$$

$$
\mathbf{B} \cdot \nabla(n_z w) = - \mathbf{B} \times \nabla \psi \cdot \nabla(n_z B^{-2}).
\tag{9}
$$

The functions u, w are evaluated numerically from the magnetic geometry and n_z; the flux-surface constants c_1 to c_4 are integrated numerically.

From (3), we obtain the (Z-normalized) peaking factor of N_z by solving for the $-\frac{1}{Z}\frac{\mathrm d \ln N_z}{\mathrm d r_{\mathrm N}}$ that gives $\langle \mathbf{\Gamma}_z \cdot \nabla r_{\mathrm N} \rangle = 0$. Denoting this peaking factor by $\mathcal{P}$, we obtain

$$
\begin{aligned}
\mathcal{P} = & - \frac{D_\Phi}{D_{N_z}}\frac{e}{T}\frac{\mathrm d \langle \Phi \rangle}{\mathrm d r_{\mathrm N}} + \frac{D_{n_i}}{D_{N_z}}\frac{\mathrm d \ln n_i}{\mathrm d r_{\mathrm N}} + \frac{D_{T_i}}{D_{N_z}}\frac{\mathrm d \ln T}{\mathrm d r_{\mathrm N}} \\
= & \left(1 + \frac{D_{n_i}}{D_{N_z}} \right)\frac{e}{T}\frac{\mathrm d \langle \Phi \rangle}{\mathrm d r_{\mathrm N}} + \frac{D_{n_i}}{D_{N_z}}\frac{\mathrm d \ln n_i}{\mathrm d r_{\mathrm N}} + \frac{D_{T_i}}{D_{N_z}}\frac{\mathrm d \ln T}{\mathrm d r_{\mathrm N}}.
\end{aligned}
\tag{10}
$$

3

The above definition of the peaking factor makes the problem independent of Z, but differs from the conventional definition of the peaking factor by a factor $1/Z$. As a result, the peaking of the actual N_z profile for a given value of $\mathcal{P}$ increases with Z. Thus, even modest reductions in $\mathcal{P}$ can lead to large reductions in the core impurity content for large Z.

To find the n_z that minimizes impurity accumulation, we can minimize $\mathcal{P}$ which, according to (10), is equivalent to minimizing a weighted sum of D_{n_i}/D_{N_z} and D_{T_i}/D_{N_z}. This picture can be further simplified, as we often find that $D_{T_i} \approx -0.5 D_{n_i}$ to within a few percent[14,20]. As a reference, we note that $D_{T_i} = -\frac{1}{2} D_{n_i}$ is exact for n_z that are constant on the flux-surface, and that only the third terms in (5) and (6) cause deviation from this exact relation.

With this approximation,

$$\mathcal{P} \approx \frac{e}{T} \frac{\mathrm{d}\langle \Phi \rangle}{\mathrm{d}r_\mathrm{N}} + \frac{D_{n_i}}{D_{N_z}} X, \tag{11}$$

where we have defined X to be the combined thermodynamic force

$$X \equiv \left(\frac{e}{T} \frac{\mathrm{d}\langle \Phi \rangle}{\mathrm{d}r_\mathrm{N}} + \frac{\mathrm{d}\ln n_i}{\mathrm{d}r_\mathrm{N}} - \frac{1}{2} \frac{\mathrm{d}\ln T}{\mathrm{d}r_\mathrm{N}} \right). \tag{12}$$

Thus, minimizing the peaking factor becomes equivalent to either maximizing or minimizing D_{n_i}/D_{N_z}, depending on the sign of X. When X is far from zero, we hence expect the n_z that optimizes the peaking factor to be insensitive to the radial gradients. This is potentially useful, as it would be cumbersome to calculate an ambipolar electric field for each n_z in the optimization loop for a non-trace impurity, and the above approximation can be verified *a posteriori* at each optimization step. We will however not do so in this work, but merely use the above argument to motivate why our optimized n_z is not very sensitive to the specific values of the gradients in (10).

Note that while the optimized n_z is insensitive to the gradients, the actual value of the peaking factor evaluated at this n_z is sensitive to the gradients.

A. Optimization

To avoid impurity accumulation, we seek to find an impurity density n_z that minimizes (10). We restrict the problem to a finite number of degrees of freedom by expressing n_z in terms of a truncated Fourier-expansion

$$\begin{aligned} n_z(\theta,\zeta) = &a_{00} f_{00}(\theta,\zeta) + \sum_{n=1}^{N} [a_{n0} f_{n0}(\theta,\zeta) + b_{n0} g_{n0}(\theta,\zeta)] \\ &+ \sum_{n=-N}^{N} \sum_{m=1}^{M} [a_{nm} f_{nm}(\theta,\zeta) + b_{nm} g_{nm}(\theta,\zeta)], \end{aligned} \tag{13}$$

where the basis functions

$$f_{nm}(\theta,\zeta) = 1 + \epsilon + \cos\left(m\theta - N_\mathrm{p} n\zeta\right), \tag{14}$$
$$g_{nm}(\theta,\zeta) = 1 + \epsilon + \sin\left(m\theta - N_\mathrm{p} n\zeta\right), \tag{15}$$

are chosen to be strictly positive ($\epsilon > 0$, here $\epsilon = 10^{-6}$), as the transport coefficients in (4)–(7) diverge for $n_z = 0$. Here, θ (ζ) is the poloidal (toroidal) Boozer angle[21,22], with N_p the number of toroidal periods of the stellarator. Thus, we restrict ourselves to impurity densities that have the same discrete rotational symmetry as the magnetic field. To avoid unrealistically sharp variation in n_z and to limit the dimensionality of the problem, we restrict ourselves to $N = M = 3$, which corresponds to 49 Fourier coefficients to optimize.

We eliminate one of the degrees of freedom, the $m = n = 0$ mode, by specifying $\langle n_z \rangle$ on the flux-surface. The state-vector of the problem thus consists of the 48 unconstrained
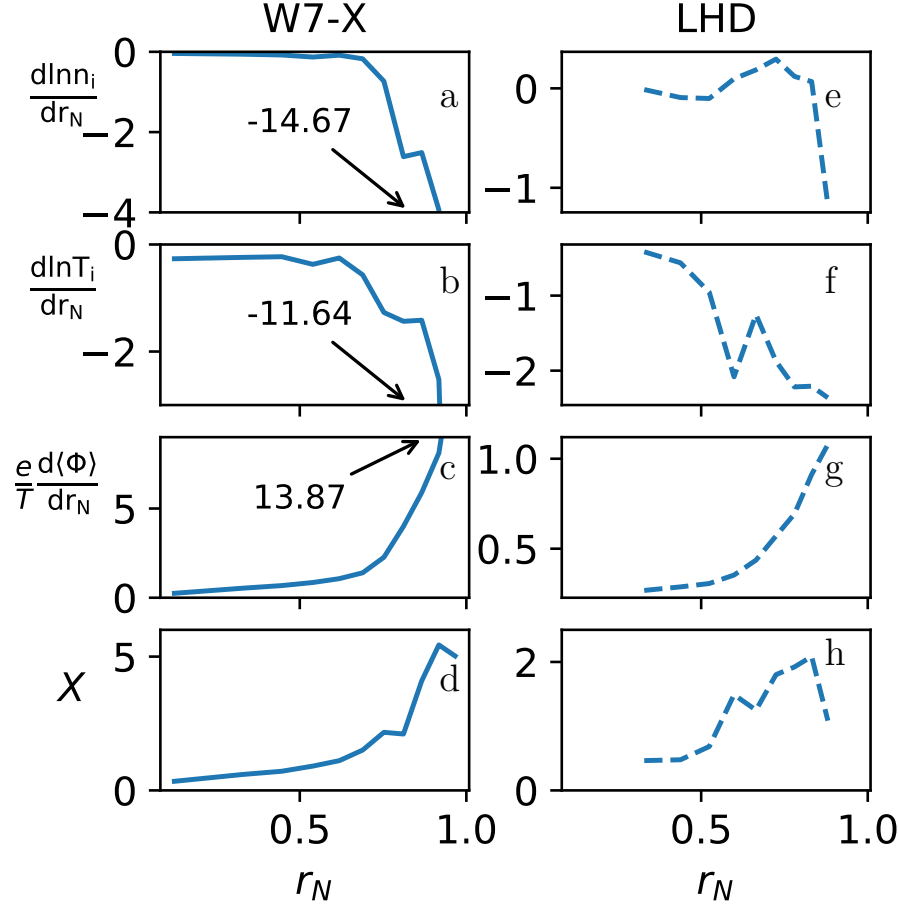
FIG. 1: Profile gradients of the W7-X (solid line) and LHD (dashed) case under consideration. The arrows indicate the values at the outermost radial point. The quanitity X is defined in (12). As X is positive, minimizing the peaking factor should correspond to minimizing D_{n_i}/D_{N_z}.

Fourier-modes. We furthermore will enforce $n_z > n_z^{\text{floor}} \geq 0$, which imposes a non-linear constraint on the Fourier-coefficients. The value of n_z^{floor} can be tuned to restrict n_z to a realistic range of values; the effect of changing n_z^{floor} is investigated in appendix A.

The optimization proceeds from an initial state-vector from which we find a *local optimum* by applying the gradient-based *method-of-moving-asymptotes*[23], as implemented in the python version of the non-linear optimization package NLOPT[24].

III.   RESULTS

We optimize n_z for a W7-X and an LHD model case, with the logarithmic and potential gradients shown in Fig. 1 and magnetic geometry in Fig. 2 and Fig. 3. The gradients in the LHD case are taken from Ref. 26, while the W7-X gradients are from a simulated case in Ref. 26. The magnetic geometries are of a W7-X standard vacuum configuration[1] and

----

[1] W7-X standard configuration available at (Verified 2019-02-15)
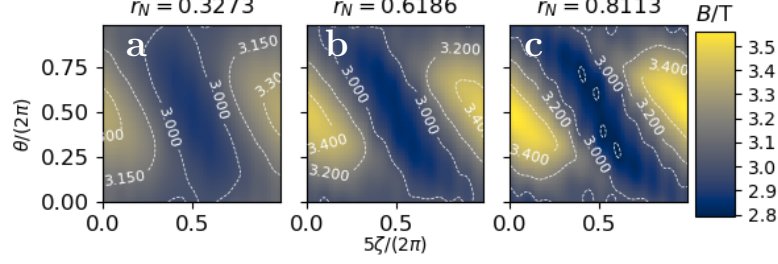   `https://github.com/landreman/sfincs/blob/master/equilibria/w7x-sc1.bc`

FIG. 2: Magnetic field strength B for a W7-X standard configuration vacuum case over one field period.
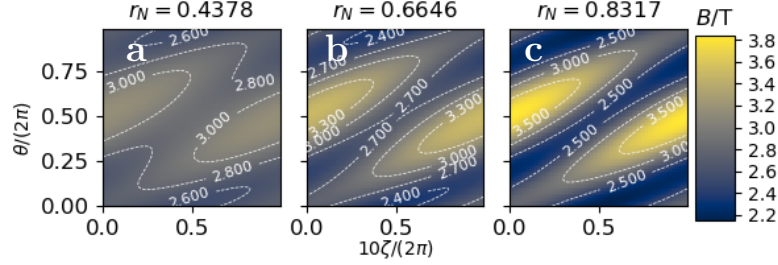

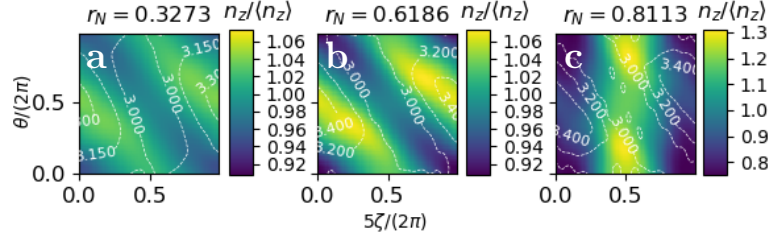FIG. 3: Magnetic field strength B for the LHD case[25,26] over one field period.

FIG. 4: n_z optimized for minimum peaking factor, for the W7-X cases in Fig. 2. The contours visualize the magnetic field at each flux-surface.
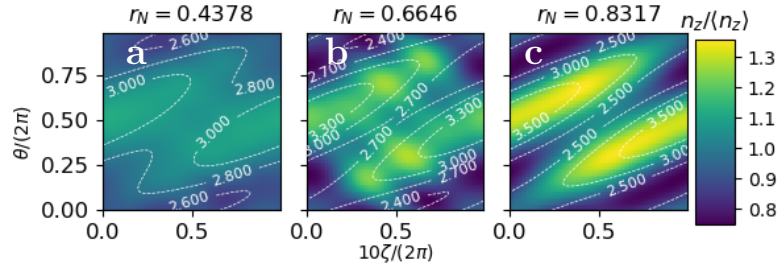

FIG. 5: Figure corresponding to Fig. 4, but for the LHD case.

from LHD discharge #113208 at $t = 4.64\,\mathrm{s}$[25,26]. Note that the cases considered here are not experimental cases, and merely use simulated or experimental data as realistic inputs.

From the last subfigure in Fig. 1, we see that $\left(\frac{e}{T} \frac{\mathrm{d}\langle\Phi\rangle}{\mathrm{d}r_\mathrm{N}} + \frac{\mathrm{d}\ln n_i}{\mathrm{d}r_\mathrm{N}} - 0.5 \frac{\mathrm{d}\ln T}{\mathrm{d}r_\mathrm{N}} \right) > 0$, which suggests that optimizing n_z to minimize either the peaking factor $\mathcal{P}$ or D_{n_i}/D_{N_z} are approximately equivalent. The optimizations start from an initially homogeneous (i.e. flux-surface constant) n_z, and we restrict the flux-surface variations to $n_z > 0.75\langle n_z\rangle$, corresponding to $n_z^{\mathrm{floor}} = 0.75\langle n_z\rangle$.

The results of such an optimization for three different radii are shown in Fig. 4 and Fig. 5, for the W7-X case and the LHD case, respectively. We see that the amplitude of the optimized n_z appears to increase with radius. For the W7-X case, the shape of the optimized n_z are qualitatively different below and above $r_N \approx 0.62$. The corresponding potential variations are presented in appendix B. In both the LHD and W7-X for $r_N < 0.62$, the optimized n_z are larger along the ridges of the maximum B, and peaking some distance away from the maximum value of B – sometimes with a second peak at the maximum of B.

To evaluate the usefulness of targeting these optima, we need to know how much they reduce the peaking factor. This is shown in Fig. 6a and Fig. 7a, for the W7-X and LHD cases. As seen in Fig. 6a, the optimization only slightly reduces the peaking factor (red curve) compared to the homogeneous case (black) in the W7-X case. The difference between the optimized and homogeneous peaking factor, $|\mathcal{P}_{\mathrm{opt}} - \mathcal{P}_{\mathrm{homo}}|$, shown in Fig. 6b, is less than 0.1 for $r_N < 0.69$, and is dwarfed by the large peaking factor in the edge. For the LHD case, the optimization yields a $|\mathcal{P}_{\mathrm{opt}} - \mathcal{P}_{\mathrm{homo}}|$ of at least 0.3, and hence has a larger impact on the impurity accumulation in the core. This decrease is from an already negative $\mathcal{P}_{\mathrm{homo}}$, which is due to difference in the geometry between the W7-X and LHD case.

In both cases, an unoptimized n_z can result in a more peaked impurity profile, as seen from the pessimized curves in Fig. 6a and Fig. 7a – which were obtained by maximizing, rather than minimizing, the peaking factor, where again we start from an initially homogeneous n_z. For the W7-X case, the effect of the pessimization is typically greater than the effect of optimization, with $\mathcal{P}_{\mathrm{pes}} - \mathcal{P}_{\mathrm{homo}} > 0.3$ for all radius, while for the LHD case, $\mathcal{P} - \mathcal{P}_{\mathrm{homo}}$ is comparable for optimization and pessimization, and ranges between 0.3 to 1.0. This appears consistent with the findings in Refs. 13,26,27, where the transport of impurities tends to be more inwards when the effect of n_z variation (through the electrostatic potential variation) is accounted for. It may also be consistent with Ref. 16, where a beneficial effect of flux-surface variation is observed in simulations of the LHD.

In Fig. 6c and Fig. 7c, we show the maximum deviations of n_z from the flux-surface value

$$\Delta n_z = \max_{\zeta,\theta} \left(\left| \frac{n_z(\zeta,\theta)}{\langle n_z \rangle} - 1 \right| \right), \tag{16}$$

which illustrates that the amplitude of n_z increases with radius, and that the nature of the optimized n_z changes above $r_N \approx 0.62$ in the W7-X case, when a solution is found with much larger amplitude ($\Delta n_z \approx 0.30$, compared to $\Delta n_z = 0.09$ for $r_N \approx 0.62$). A similarly large amplitude also occurs at a lower, isolated radius ($r_N = 0.52$) with no noticeable change in the peaking factor, indicating that the two kinds of optima have very similar peaking factors around these radii. This shows that at least $\Delta n_z \sim 0.3$ variations can exist without severely impacting the peaking factor. On the other hand, the pessimized n_z tend to have larger Δn_z in both the W7-X and LHD case.

A.   Influence of small-amplitude modes

For the optimized n_z to be reasonable targets in an experiment, they must be robust to small changes. We investigate this by considering how many of the 48 unconstrained Fourier modes actually contribute to lowering the peaking factor.

We investigate this by zeroing out Fourier-coefficients below a threshold value in our representation of n_z, (13). The resulting change in peaking factor and the number of retained unconstrained modes is shown in Fig. 8 and Fig. 9, for the W7-X and LHD case at two different radii, which are representative of the behaviour in the core and the edge. Note that the constrained $m = 0, n = 0$ cosine mode is always retained, and is set by the other modes to ensure that $\langle n_z \rangle$ is held constant. Also note the linear scale in the number of retained modes below 10 in Fig. 8 and Fig. 9, and the logarithmic scale when more than 10 modes are retained. For all cases, less than 10 modes actually contribute to visibly reducing the peaking factor, as seen by the constant peaking factor for low values of the
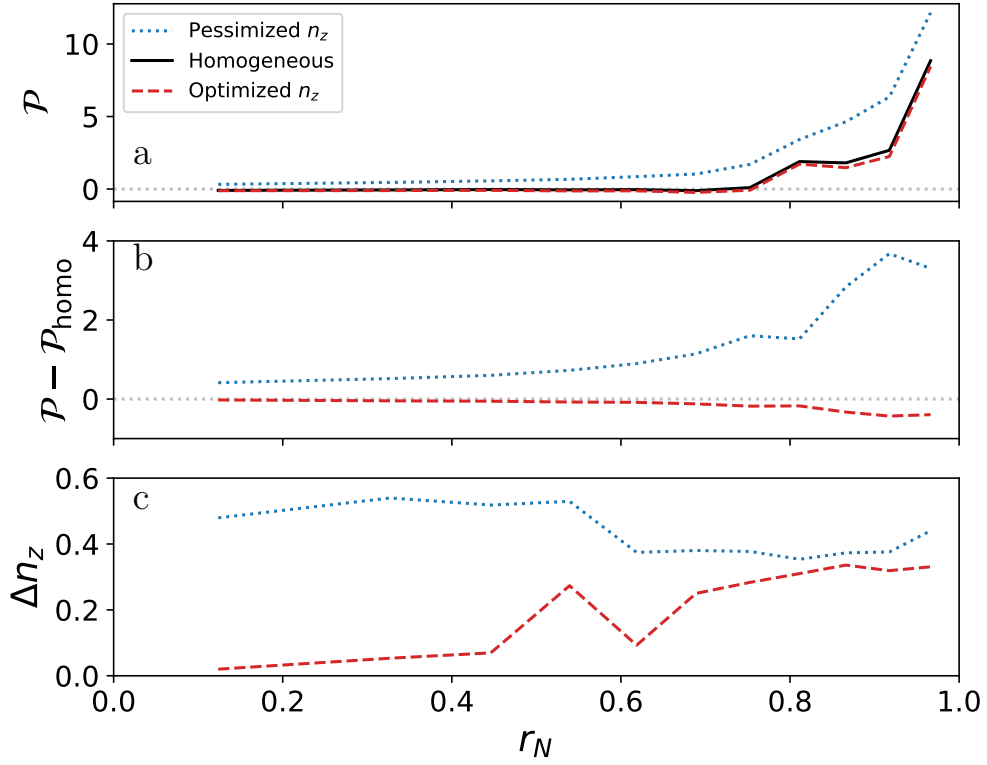
FIG. 6:   **a:** peaking factor at different radii for the W7-X case. **b:** Differential change in peaking factor compared to the homogeneous case. **c:** The maximum deviation in $n_z/\langle n_z \rangle$.
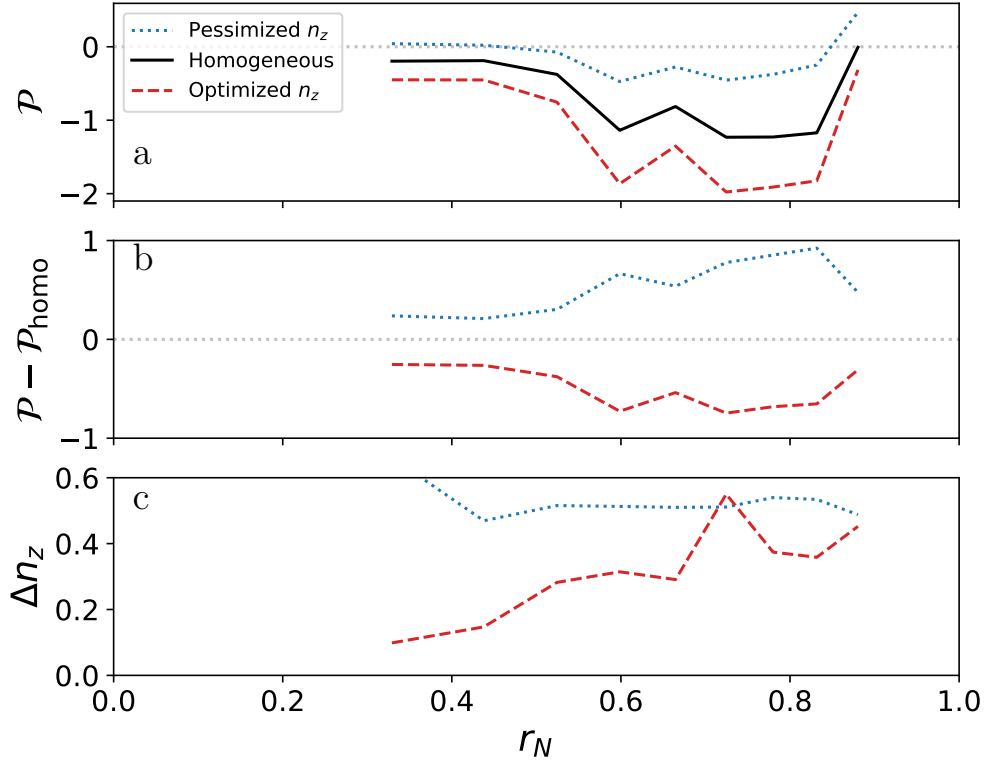

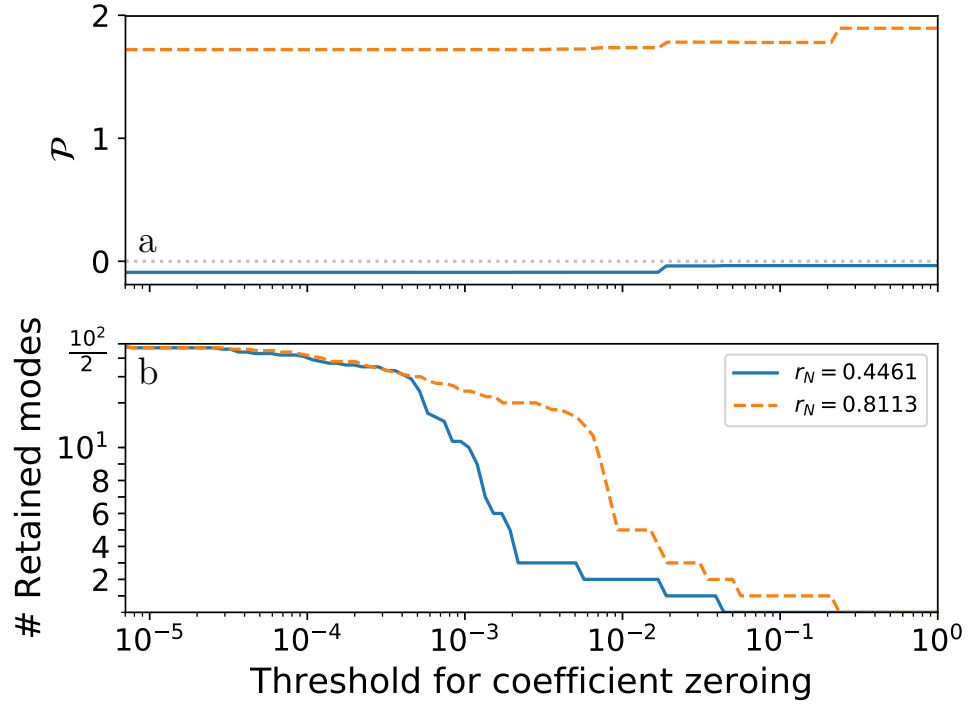FIG. 7:   Figure corresponding to Fig. 6, for the LHD case.

FIG. 8:   The effect of zeroing out coefficients below a threshold value on the peaking factor $\mathcal{P}$ in the W7-X case.
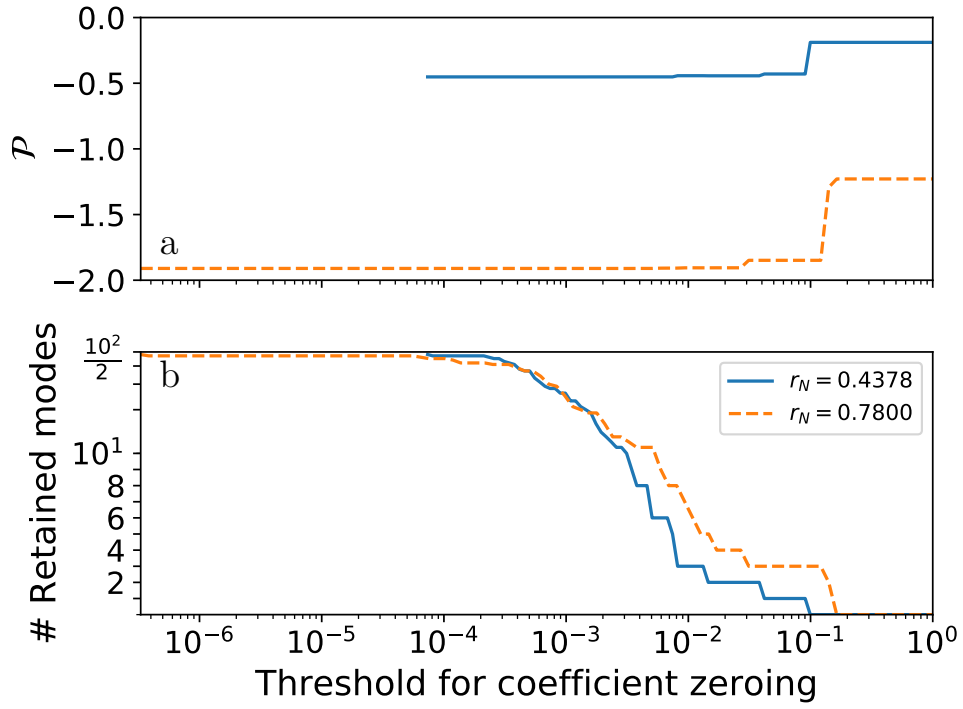

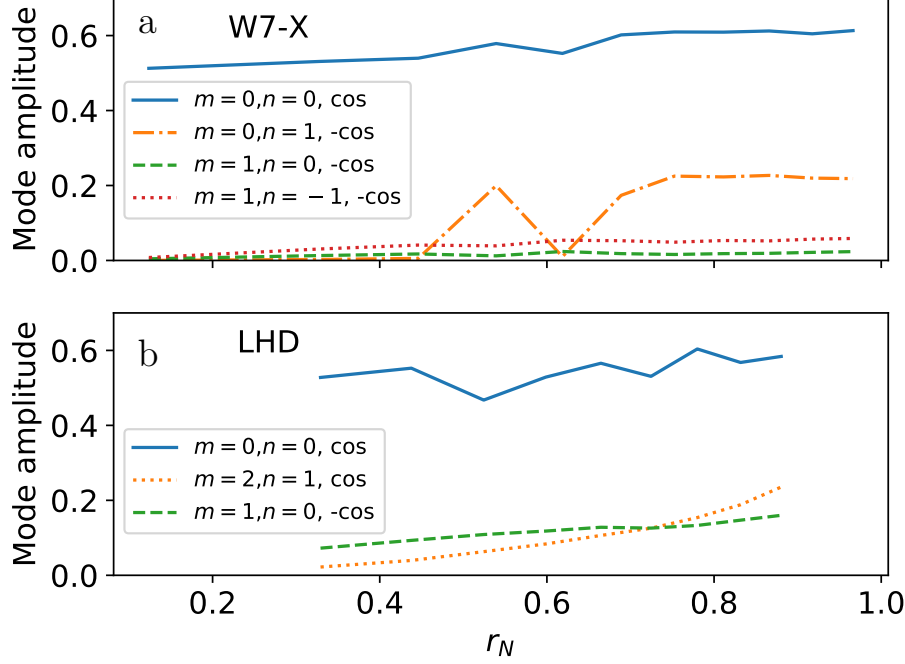
FIG. 9:   Figure corresponding to Fig. 8 for the LHD case.

FIG. 10: Dominant modes for the different radii in the W7-X and LHD cases. Modes
with negative amplitudes are marked with a "−" in the legend.

zeroing-threshold. In fact, the sharpest increase in the peaking factor occurs only when the
last one or two unconstrained modes are zeroed out. For the W7-X case, this sharp increase
occurs when the last two (last) unconstrained mode is zeroed in the core (edge), while in
the LHD case it occurs at the last (last two) in the core (edge). Retaining only the two
largest modes, 92% (90%) of the optimization in $\mathcal{P}_{\mathrm{opt}} - \mathcal{P}_{\mathrm{homo}}$ is retained in the LHD core
(edge), while the corresponding number in the W7-X case is 99% (66%). This shows that
only one or two dominant unconstrained modes are needed for most of the optimization.

   To illustrate which two modes are the dominant ones, we plot the amplitude of the
relevant modes against radius in Fig. 10, alongside the constrained $m = 0, n = 0$ mode.
From the W7-X subfigure in Fig. 10, we clearly see that the nature of the optimized n_z
changes for $r_N > 0.62$, but it transitions temporarily already at $r_N \approx 0.54$, as previously
observed. In the LHD case, the $m = 1, n = 0$ cosine mode is the dominant unconstrained
mode at low r_N, but the $m = 2, n = 1$ cosine mode overtakes it at $r_N \approx 0.7$. In both cases,
no sine modes contribute significantly to the optimization; sine modes appear to increase
the peaking factor in the cases considered here.

   By restricting our attention only to the two dominant modes, we can visualize the opti-
mization landscape to identify the globally optimal amplitudes for these modes. For this
purpose, we perform a two-dimensional scan in the amplitudes of the dominant modes for
the W7-X and LHD cases. For the W7-X case, we restrict our attention to the two dominant
modes at low r_N.

   The peaking factor for each point in this scan is illustrated in Fig. 11 and Fig. 12, for
the W7-X and LHD case, respectively. The contour lines represent the limit imposed by
the optimization requiring $n_z/\langle n_z \rangle > 0.75$. From these figures, we see that the optimum
(red dot) tends to higher amplitudes for higher r_N, and also that it is the local optimum
starting from an initially homogeneous n_z (green dot). The root mean square (RMS) of the
amplitudes $\left(\sqrt{a_x^2 + a_y^2}/\langle n_z \rangle \right)$ scale linearly with r_N: for the W7-X case, the RMS amplitude
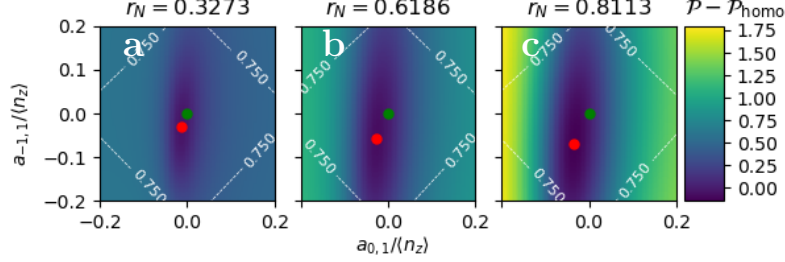
FIG. 11: The differential peaking factor $\mathcal{P} - \mathcal{P}_{\mathrm{homo}}$ at each point in an amplitude scan of the two dominant modes at low r_N in the W7-X optimization. Note that these two modes are not dominant in the previously found optima at $r_N > 0.62$, see the W7-X subfigure of Fig. 10. The red dot indicates the location of the minimum, and the green dot a homogeneous n_z.
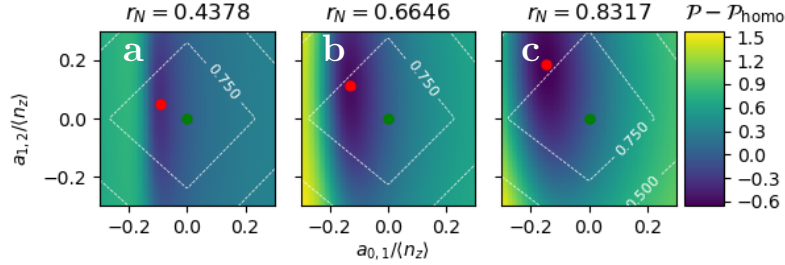

FIG. 12: A figure corresponding to Fig. 11, for the LHD case.

at the different radii are 0.033, 0.061, and 0.079, respectively, while they are 0.107, 0.172, and 0.237 for the LHD case. In both the W7-X and LHD case, the optimum is relatively narrow in the amplitude of the $m = 1, n = 0$ cosine mode (x-axis), but broadens for higher r_N.

Regardless of how narrow the optimum is, it is always beneficial to have an $m = 1, n = 0$ cosine mode of moderate amplitude, compared to the homogeneous case, but the peaking factor rapidly increases when the amplitude becomes larger than a threshold value. For the W7-X case, the threshold values at these radii are -0.02, -0.038 and -0.055; and for the LHD case, they are -0.13, -0.19 and -0.22. The peaking factor is less sensitive to the amplitude of the other mode ($m = 1, n = -1$ in W7-X; $m = 2, n = 1$ in LHD), but the minima in these broader basins nevertheless tend towards larger amplitudes at higher r_N. For the LHD case, the amplitude of the minima becomes sufficiently large to hit the $n_z > 0.75\langle n_z \rangle$ constraint, which we imposed to exclude large n_z variation.

B.   Reduction in core density

The peaking factor can be integrated to yield the impurity pseudo-density profile

$$\left(\frac{N_z(r_N)}{N_z(r_N^{\mathrm{edge}})} \right)^{1/Z} = \exp \left(\int_{r_N}^{r_N^{\mathrm{edge}}} \mathcal{P}(r_N') \, \mathrm{d}r_N' \right), \qquad (17)$$

which allows us to assess how effective the optimization is in reducing the core impurity density. To perform the above integral numerically, we optimized the peaking factor for 97 radii in the W7-X case, and 47 radii in the LHD case, using the same modes as in Fig. 11 and Fig. 12 for the respective cases.

The resulting N_z profiles are shown in Fig. 13. Thus, the optimization reduces $(N_z(r_N^{\mathrm{core}})/N_z(r_N^{\mathrm{edge}}))^{1/Z}$ to 89% of the homogeneous n_z value, from 2.00 to 1.78, in the W7-X case; and to 75%,
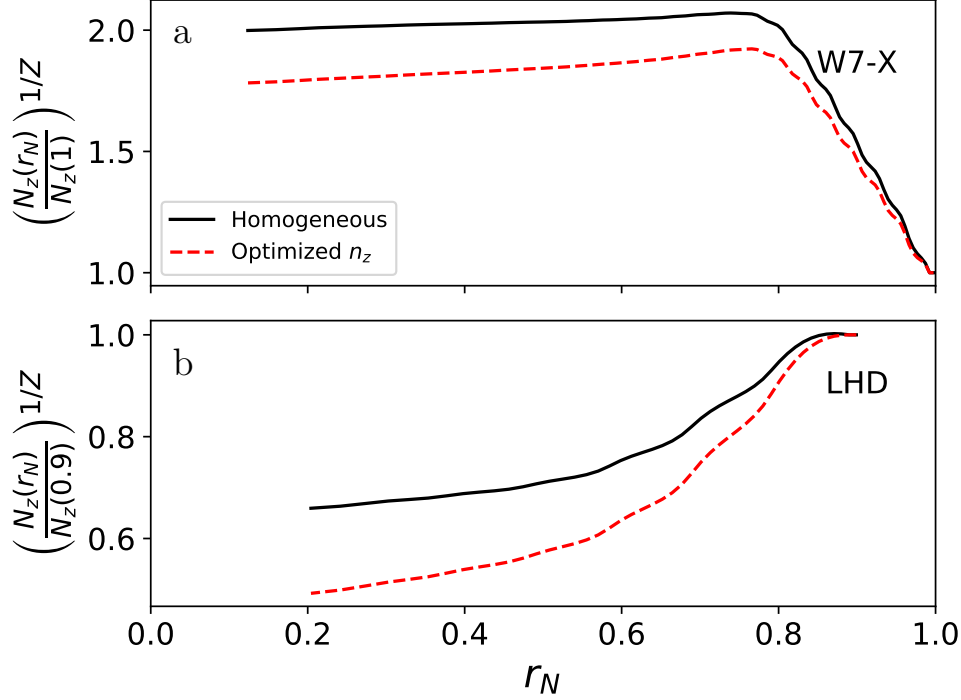
FIG. 13: The steady-state impurity psuedo-density profiles $N_Z(r_N)$ for n_z constant on the flux-surface (homogeneous) or n_z optimized to minimize the peaking factor, for the W7-X case (a) and LHD case (b). The optimizations used the same modes as in Fig. 11 and Fig. 12 for the respective cases.

from 0.659 to 0.492, in the LHD case. The corresponding reduction in the pseudo-density is exponentiated by Z: At $Z = 24$, the optimization reduces the W7-X core impurity content to 6% of the unoptimized levels, while for the LHD case, the corresponding reduction is to 0.09% of the unoptimized levels. This shows that even modest reductions in $\mathcal{P}$ can yield large reductions in the impurity density at sufficiently large Z.

IV.   SUMMARY & CONCLUSIONS

We have performed numerical optimizations of the impurity density variation on the flux-surface, $n_z(\zeta, \theta)$, to minimize a semi-analytical expression for the impurity pseudo-density peaking factor, valid in the *mixed-collisionality regime* with a collisional impurity of charge $Z \gg 1$ and a low-collisionality bulk-ion species. In order to constrain n_z to a realistic range of variations, we have only performed local optimizations of n_z around a homogeneous initial value, using a gradient-based minimization method to minimize the peaking factor. To further constrain n_z, we have imposed $n_z > 0.75\langle n_z \rangle$, as the optimization otherwise can produce unrealistically large n_z variations on the flux-surface.

The results show that there is a potential to lower the Z-normalized impurity peaking factor by 0.3 by controlling n_z in the LHD case considered here, while the optimization in the W7-X case lowers the Z-normalized peaking factor by 0.1 compared to a homogeneous n_z. On the other hand, we find that there are flux surface variations that lead to a ~ 2.0 increase in the Z-normalized impurity peaking factor in both the W7-X and LHD case. In both cases, the reduction in peaking factor can lead to significant reduction in the core density for sufficiently high impurity charge, with the ratio of optimized to homogeneous

core densities being given by $N_z^{\mathrm{opt}}/N_z^{\mathrm{homo}} = 0.89^Z$ in the W7-X case and 0.75^Z in the LHD case considered here.

In conclusion, this study shows that it may be worthwhile to experiment with n_z variation in stellarators to reduce core impurity accumulation. The fact that only one or two modes of low mode-numbers are required to optimize the impurity density is promising, and could provide signatures of optimized impurity variations that may be targetable (by for example heating[12,16] or tailoring the magnetic field[15]) and measurable in experiments, using for example Doppler reflectometry[28] or probes[29]. In particular, it appears that $m = 1, n = 0$ cosine modes of moderate amplitudes (up to $-0.07\langle n_z \rangle$ to $-0.22\langle n_z \rangle$, with larger amplitudes at larger radius) are beneficial in the LHD case considered here. For the W7-X standard configuration, the n_z optimization is less effective in reducing the peaking factor, and from this perspective, it may be wise to avoid n_z variations. On the other hand, there exist n_z variations with large amplitudes and slightly-better than homogeneous performance in W7-X, so n_z variations are not intrinsically harmful. Furthermore, at high enough Z, even a moderate reduction in peaking factor leads to a significant reduction in core density. It is however unclear how these results extrapolate to different magnetic configurations, as this study is of limited scope. Furthermore, the D_{N_z} coefficient may be modified by the presence of turbulent transport[30], which should affect the results. These are interesting avenues for future work.

Appendix A: Effects of changing the minimum n_z value

In the bulk of this paper, we optimized n_z given the constraint $n_z > 0.75\langle n_z \rangle$. Here, we show the effects of lifting that constraint, to demonstrate why a constraint of this sort is necessary.

In Fig. 14a and Fig. 15a, we show the optimized n_z obtained for the flux-surfaces in Fig. 2 and Fig. 3, by the optimization procedure described in Sec. II A starting from an initially homogeneous n_z and only requiring $n_z > 0$ everywhere on the flux-surface.

From these figures, we see that when the amplitude of the optimized n_z is allowed to increase, the optimization algorithm starts to find a new kind of local minimum, with unrealistically large amplitude, a radically different shape, and no clear correlation to the magnetic field strength. This occurs at $r_N > 0.62$ in the W7-X case, and already at $r_N > 0.33$ in the LHD case.

Thus, without specifying a lowest allowed value for n_z, even optimizations starting from a homogeneous initial n_z cannot be guaranteed to display reasonable n_z variations. The shape of the optima found at the outer radii in Fig. 14a is in fact very similar to a "global" optimum obtained by stochastic optimization where several initial n_z are randomly generated and the lowest local optimum resulting from performing local optimization from these initial n_z's is taken as an upper bound for the global minimum. The result of this process for $r_N = 0.6$ in W7-X is shown in Fig. 16. The situation in the W7-X case may thus be illustrated as
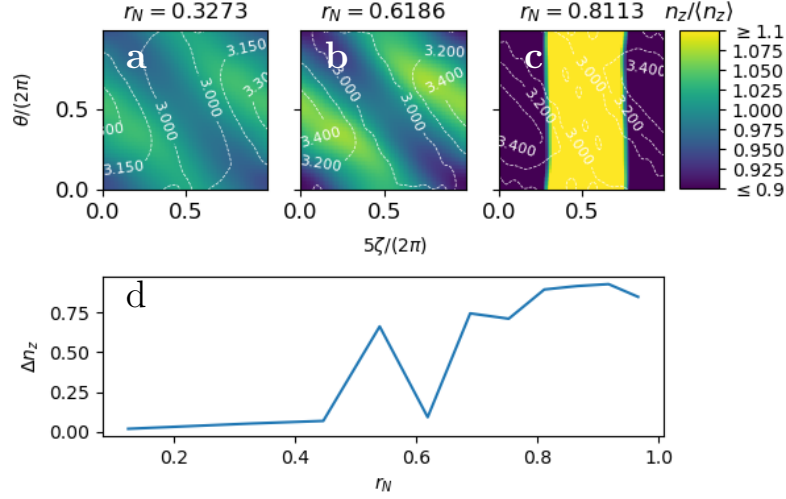
FIG. 14: **a-c:** n_z optimized for minimum peaking factor with $n_z > 0$, for the W7-X cases in Fig. 2. The contours visualize the magnetic field at each flux-surface. **d:** Δn_z for each flux-surface.
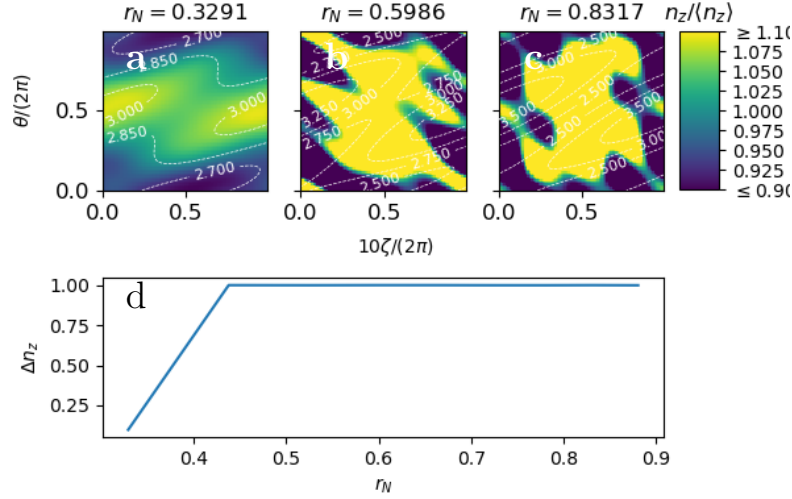

FIG. 15: Figure corresponding to Fig. 14, but for the LHD case.

in Fig. 17, where there always exist local minima unrealistically far from a homogeneous n_z that are more optimal than those obtained from starting the local optimization at a homogeneous n_z.

This is the reason for optimizing on a more restrictive function-space, for example by specifying $n_z > n_z^{\text{floor}}$ for some n_z^{floor}. A better approach would be to restrict n_z to a function-space of "reasonable" impurity density variations based on the physical modeling of the phenomena causing the flux-surface variation, but this is outside the scope of this work.
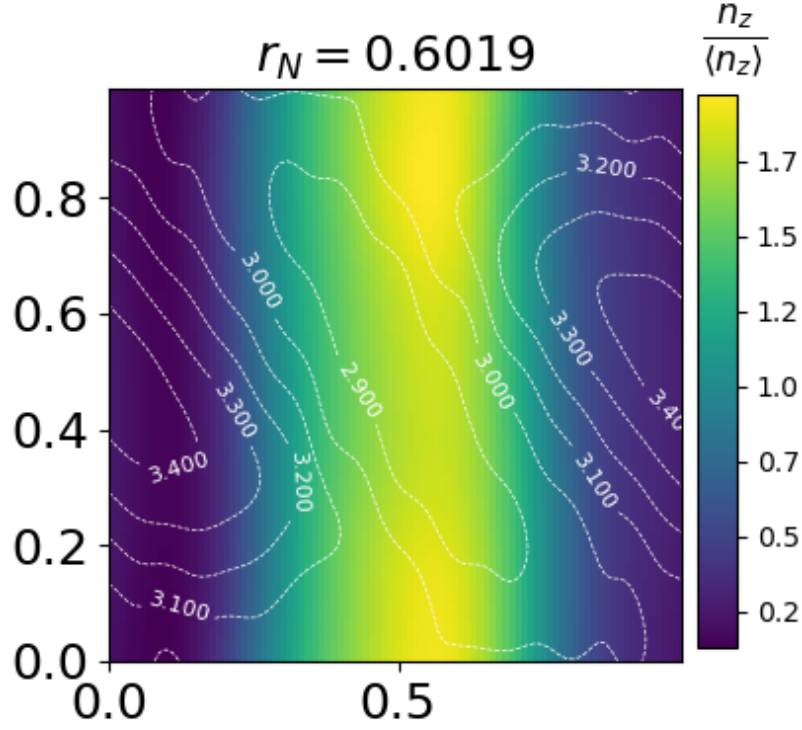
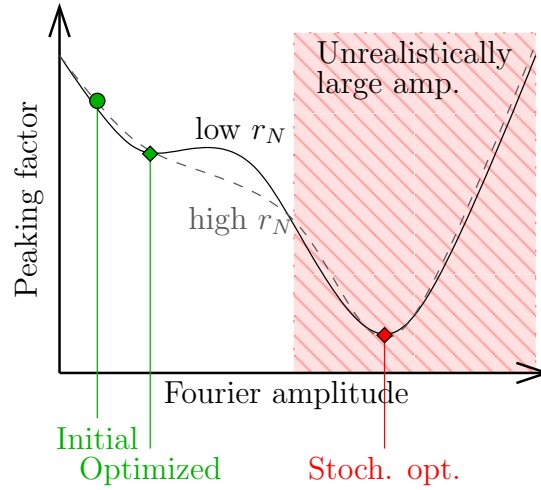FIG. 16: Optimized n_z resulting from stochastic optimization in the W7-X case at $r_N = 0.6$.

FIG. 17: Illustration of the local optimization landscape in the W7-X case, for two different radii. At higher r_N, a local optimizer starting at a uniform n_z finds an optimum that was inaccessible but existed at lower r_N; as revealed by the stochastic optimization. The differences in peaking factor are here exaggerated for illustrative purposes.
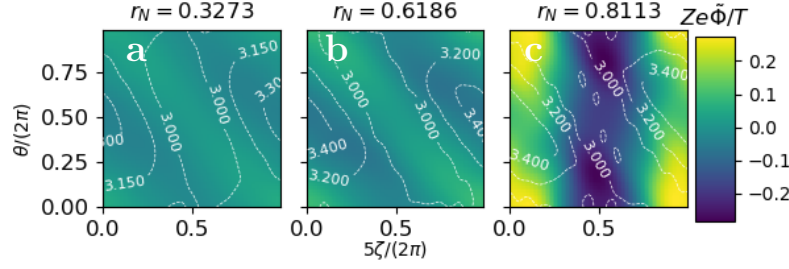
FIG. 18: $\tilde{\Phi}$ corresponding to the W7-X n_z in Fig. 4, which is optimized for minimum peaking factor, for the W7-X cases in Fig. 2. The contours visualize the magnetic field at each flux-surface.
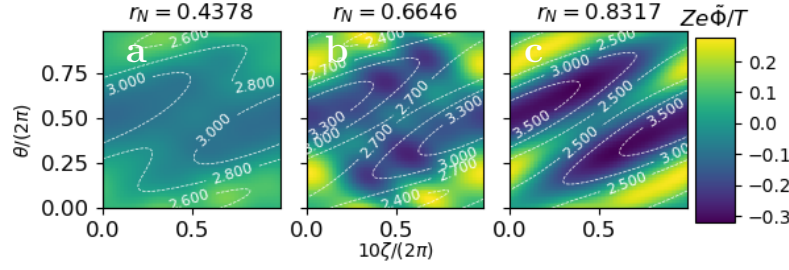

FIG. 19: Figure corresponding to Fig. 18 for the LHD case, showing the $\tilde{\Phi}$ due to the n_z in Fig. 5.

Appendix B: Corresponding potential variation

In this work, we calculate n_z that optimize the impurity peaking factor, with little regard for the physical mechanisms that set n_z. However, physics-based calculations of n_z often calculate flux-surface variation of the electrostatic potential, from which n_z is obtained through (2). To connect our results to previous theoretical studies, we thus invert (2) to obtain $\tilde{\Phi}$'s corresponding to our optimized n_z

$$\frac{Ze\tilde{\Phi}}{T} = -\log n_z + C, \tag{B1}$$

where C is a constant calculated to make $\langle\tilde{\Phi}\rangle = 0$. The resulting $Ze\tilde{\Phi}/T$ for the W7-X and LHD cases are displayed in Fig. 18 and Fig. 19.

[1]S. Sudo, "A review of impurity transport characteristics in the LHD," Plasma Physics and Controlled Fusion **58**, 043001 (2016).

[2]L. Giannone, J. Baldzuhn, R. Burhenn, P. Grigull, U. Stroth, F. Wagner, R. Brakel, C. Fuchs, H. J. Hartfuss, K. McCormick, A. Weller, C. Wendland, NBI Team, ECRH Team, W7-AS Team, K. Itoh, and S.-I. Itoh, "Physics of the density limit in the W7-AS stellarator," Plasma Physics and Controlled Fusion **42**, 603 (2000).

[3]Y. Nakamura, Y. Takeiri, B. J. Peterson, S. Muto, K. Ida, H. Funaba, M. Yokoyama, K. Narihara, Y. Nagayama, S. Inagaki, T. Tokuzawa, S. Morita, M. Goto, K. Sato, M. Osakabe, S. Masuzaki, H. Suzuki, R. Kumazawa, T. Mutoh, T. Shimozuma, M. Sato, N. Noda, K. Kawahata, N. Ohyabu, O. Motojima, and The LHD Experimental Group, "Impurity behaviour in LHD long pulse discharges," Plasma Physics and Controlled Fusion **44**, 2121 (2002).

[4]R. Burhenn, Y. Feng, K. Ida, H. Maassberg, K. McCarthy, D. Kalinina, M. Kobayashi, S. Morita, Y. Nakamura, H. Nozato, S. Okamura, S. Sudo, C. Suzuki, N. Tamura, A. Weller, M. Yoshinuma, and B. Zurro, "On impurity handling in high performance stellarator/heliotron plasmas," Nuclear Fusion **49**, 065005 (2009).

[5]M. Yokoyama, H. Maaßberg, C. Beidler, V. Tribaldos, K. Ida, T. Estrada, F. Castejon, A. Fujisawa, T. Minami, T. Shimozuma, Y. Takeiri, A. Dinklage, S. Murakami, and H. Yamada, "Core electron-root confinement (CERC) in helical plasmas," Nuclear Fusion **47**, 1213–1219 (2007).

[6]A. Sagara, Y. Igitkhanov, and F. Najmabadi, "Review of stellarator/heliotron design issues towards MFE DEMO," Fusion Engineering and Design **85**, 1336 – 1341 (2010), proceedings of the Ninth International Symposium on Fusion Nuclear Technology.

[7]P. Helander, S. L. Newton, A. Mollén, and H. M. Smith, "Impurity transport in a mixed-collisionality stellarator plasma," Phys. Rev. Lett. **118**, 155002 (2017).

[8]S. Braun and P. Helander, "Pfirsch-Schlüter impurity transport in stellarators," Physics of Plasmas **17**, 072514 (2010), https://doi.org/10.1063/1.3458901.

[9]S. L. Newton, P. Helander, A. Mollén, and H. M. Smith, "Impurity transport and bulk ion flow in a mixed collisionality stellarator plasma," Journal of Plasma Physics **83**, 905830505 (2017).

[10]P. Helander, "Bifurcated neoclassical particle transport," Physics of Plasmas **5**, 3999–4004 (1998), http://dx.doi.org/10.1063/1.873121.

[11]T. Fülöp and P. Helander, "Nonlinear neoclassical transport in a rotating impure plasma with large gradients," Physics of Plasmas **6**, 3066–3075 (1999), http://dx.doi.org/10.1063/1.873593.

[12]C. Angioni and P. Helander, "Neoclassical transport of heavy impurities with poloidally asymmetric density distribution in tokamaks," Plasma Physics and Controlled Fusion **56**, 124001 (2014).

[13]I. Calvo, F. I. Parra, J. L. Velasco, J. A. Alonso, and J. G.-R. na, "Stellarator impurity flux driven by electric fields tangent to magnetic surfaces," Nuclear Fusion **58**, 124005 (2018).

[14]S. Buller, H. M. Smith, P. Helander, A. Mollén, S. L. Newton, and I. Pusztai, "Collisional transport of impurities with flux-surface varying density in stellarators," Journal of Plasma Physics **84**, 905840409 (2018).

[15]I. Calvo, J. L. Velasco, F. I. Parra, J. A. Alonso, and J. M. García-Regaña, "Electrostatic potential variations on stellarator magnetic surfaces in low collisionality regimes," Journal of Plasma Physics **84**, 905840407 (2018).

[16]H. Yamaguchi and S. Murakami, "Simulation study of electrostatic potential generated by NBI and its effect on the neoclassical transport of carbon impurity ions in LHD," IAEA Fusion Energy Conference preprints, Gandhinagar, India , TH/P6–29 (2018).

[17]B. Geiger, T. Wegner, C. Beidler, R. Burhenn, B. Buttenschön, R. Dux, A. Langenberg, N. Pablant, T. Pütterich, Y. Turkin, T. Windisch, V. Winters, M. Beurskens, C. Biedermann, K. Brunner, G. Cseh, H. Damm, F. Effenberg, G. Fuchert, O. Grulke, J. Harris, C. Killer, J. Knauer, G. Kocsis, A. Krämer-Flecken, T. Kremeyer, M. Krychowiak, O. Marchuk, D. Nicolai, K. Rahbarnia, G. Satheeswaran, J. Schilling, O. Schmitz, T. Schröder, T. Szepesi, H. Thomsen, H. T. Mora, P. Traverso, D. Zhang, and The W7-X Team, "Observation of anomalous impurity transport during low-density experiments in W7-X with laser blow-off injections of iron," Nuclear Fusion **59**, 046009 (2019).

[18]T. Fülöp and S. Moradi, "Effect of poloidal asymmetry on the impurity density profile in tokamak plasmas," Physics of Plasmas **18**, 030703 (2011), https://doi.org/10.1063/1.3569841.

[19]A. Mollén, I. Pusztai, T. Fülöp, Y. O. Kazakov, and S. Moradi, "Effect of poloidal asymmetries on impurity peaking in tokamaks," Physics of Plasmas **19**, 052307 (2012), https://doi.org/10.1063/1.4719711.

[20]S. Buller, H. Smith, P. Helander, A. Mollén, S. Newton, and I. Pusztai, "Transport of collisional impurities with flux-surface density variation in stellarator plasmas," IAEA Fusion Energy Conference preprints, Gandhinagar, India , TH/P6–13 (2018).

[21]A. H. Boozer, "Plasma equilibrium with rational magnetic surfaces," The Physics of Fluids **24**, 1999–2003 (1981), https://aip.scitation.org/doi/pdf/10.1063/1.863297.

[22]P. Helander, "Theory of plasma confinement in non-axisymmetric magnetic fields," Reports on Progress in Physics **77**, 087001 (2014).

[23]K. Svanberg, "The method of moving asymptotes – a new method for structural optimization," International Journal for Numerical Methods in Engineering **24**, 359–373 (1987), https://onlinelibrary.wiley.com/doi/pdf/10.1002/nme.1620240207.

[24]S. G. Johnson, "The NLopt nonlinear-optimization package," (2018).

[25]J. Velasco, I. Calvo, S. Satake, A. Alonso, M. Nunami, M. Yokoyama, M. Sato, T. Estrada, J. Fontdecaba, M. Liniers, K. McCarthy, F. Medina, B. P. V. Milligen, M. Ochando, F. Parra, H. Sugama, A. Zhezhera, The LHD Experimental Team, and The TJ-II Team, "Moderation of neoclassical impurity accumulation in high temperature plasmas of helical devices," Nuclear Fusion **57**, 016016 (2017).

[26]A. Mollén, M. Landreman, H. M. Smith, J. M. García-Regaña, and M. Nunami, "Flux-surface variations of the electrostatic potential in stellarators: impact on the radial electric field and neoclassical impurity transport," Plasma Physics and Controlled Fusion **60**, 084001 (2018).

[27]J. García-Regaña, C. Beidler, R. Kleiber, P. Helander, A. Mollén, J. Alonso, M. Landreman, H. Maaßberg, H. Smith, Y. Turkin, and J. Velasco, "Electrostatic potential variation on the flux surface and its impact on impurity transport," Nuclear Fusion **57**, 056004 (2017).

[28]T. Estrada, D. Carralero, E. Sanchez, E. Ascasibar, I. Pastor, J. M. G.-R. na, M. Liniers, and Álvaro Cappa, "Turbulence and radial electric field asymmetries measured at TJ-II plasmas," IAEA Fusion Energy Conference preprints, Gandhinagar, India , EX/P1–9 (2018).

[29]M. Pedrosa, J. Alonso, J. García-Regaña, C. Hidalgo, J. Velasco, I. Calvo, R. Kleiber, C. Silva, and P. Helander, "Electrostatic potential variations along flux surfaces in stellarators," Nuclear Fusion **55**, 052001 (2015).

[30]P. Helander and A. Zocco, "Quasilinear particle transport from gyrokinetic instabilities in general magnetic geometry," Plasma Physics and Controlled Fusion **60**, 084006 (2018).